Chemical Engineering Journal 483 (2024) 149377

Contents lists available at ScienceDirect

Chemical Engineering Journal

journal homepage: www.elsevier.com/locate/cej

Microfluidic Tesla mixer with 3D obstructions to exceptionally improve the curcumin encapsulation of PLGA nanoparticles

Phuong Thao Le, Seung Hui An, Heon-Ho Jeong *

Department of Chemical and Biomolecular Engineering, Chonnam National University, 50 Daehak-ro, Yeosu, Jeollanam-do 59626, Republic of Korea

ARTICLE INFO

Keywords:
Microfluidic mixing
Tesla structure
3D obstruction
Drug encapsulation

ABSTRACT

Nanoprecipitation is a well-established method that involves straightforward and rapid mixing to encapsulate therapeutic drugs into polymeric nanoparticles (NPs). Microfluidic mixing has emerged as a powerful method for achieving small and uniform NPs, which are particularly challenging with conventional bulk mixing. Various geometries have been developed to enhance mixing efficiency in microfluidics. Efficient fluid mixing using Tesla structures has been successfully established, but the integration of 3D obstructions into Tesla structures has not yet been reported. Our focus is on enhancing mixing efficiency using a 3D microfluidic Tesla mixer, which was achieved by integrating 3D obstructions (triangular prism, cylinder, and cone) into Tesla structures fabricated by 3D printing. We examine the impact of the Tesla structure and geometrical characteristics of the obstructions on the flow phenomenon and chaotic mixing via computational fluid dynamics (CFD) simulations and experiments. We demonstrate that the Tesla mixer with cone-shaped obstructions significantly improves the mixing efficiency, resulting in a remarkable 99.4 % mixing index within 400 ms at a flow rate of 50 mL/h. We use the optimal 3D microfluidic Tesla mixer to control the formulation of small and uniform poly(lactic-co-glycolic) acid (PLGA) NPs by varying the solvent type, PLGA concentration and molecular weight, and flow condition. Importantly, curcumin-encapsulated PLGA NPs (Cur-PLGA NPs) with high drug encapsulation efficiency (up to 68.40 %) and exceptional curcumin loading (up to 43.01 %) are produced using our device with high mixing efficiency. Furthermore, in vitro studies on curcumin drug release with different degradation rates as pH changes reveal that our 3D microfluidic Tesla mixer has considerable potential as a scalable production device for drug delivery applications with a highly unique efficacy.

1. Introduction

Engineering drug delivery systems hold significant promise for the development of pharmaceutical products that can improve disease treatment [1–3]. One of the most interesting fields involving drug delivery systems is nanotechnology, which enables the design of drug nanocarriers with well-defined and controllable physicochemical properties, such as size, shape, porosity, and surface functionalization [4,5]. In particular, reducing the size of drug carriers to the nanometer scale can enhance their therapeutic effect by promoting the penetration of particles through gaps in the extracellular matrix or tumorous vasculature. Among the various types of nanoparticles (NPs), polymeric NPs have attracted significant interest over the past few decades because they possess considerable potential for drug delivery owing to their controllable functionalities [6,7]. Polymeric NPs can encapsulate various therapeutic molecules, such as hydrophilic DNA, protein, and hydrophobic compounds, which make up the majority of active pharmaceutical drugs. Such encapsulated drugs in functional polymeric NPs improve pharmacological properties, such as bioavailability and biological half-life, protecting them from premature deactivation through metabolism [8–10].

Among the various natural organic drug compounds that can be encapsulated in polymeric NPs, curcumin is a notable bioactive component with a wide range of important pharmacological treatment efficacy, including anticancer, anti-inflammatory, antimicrobial, antioxidant, and neuroprotective effects [11–14]. Although curcumin has significant potential to treat several diseases, it has limited bioavailability due to its poor aqueous solubility, pH-dependent degradation, and quick conversion to metabolites in the body. These challenges can be overcome by encapsulating curcumin in functional polymeric NPs with controlled release, which would increase its solubility, decrease its metabolic degradation rate, and ultimately improve its bioavailability

* Corresponding author.
E-mail address: jeonghh29@jnu.ac.kr (H.-H. Jeong).

https://doi.org/10.1016/j.cej.2024.149377
Received 30 August 2023; Received in revised form 14 January 2024; Accepted 3 February 2024
Available online 5 February 2024

and pharmacological activity.

One of the polymers that have been widely used as a drug carrier is poly(lactic-co-glycolic) acid (PLGA), which is a synthetic biodegradable polymer that decomposes into nontoxic metabolites lactic and glycolic acid monomers [15]. Synthetic PLGA is appealing because its biodegradable rate can be manipulated by tuning the molecular weight and ratio of lactic and glycolic acid, providing enhanced regulation and control of drug release. Because of this, PLGA NPs is able to reduce variations in the plasma concentration of a drug that could lead to undesired toxicity and side effects [16,17]. The encapsulated curcumin in PLGA NPs has been reported to have higher stability (half-life of 2 days) than free curcumin (half-life of 20 min) [18]. In addition, surfactant-coated PLGA NPs have shown remarkably improved stability, including long-term storage, in vitro and in vivo biodistribution and bioavailability, and cellular uptake capability [19–22]. However, advanced manufacturing technology for curcumin-encapsulated PLGA NPs (Cur-PLGA NPs) is still required to improve quality control and drug efficacy. The conventional batch-to-batch process has limited ability to improve drug efficacy because of the polydisperse size and low drug encapsulation efficiency (EE) of the produced NPs [23,24]. Thus, NP production requires strict control of physicochemical properties, such as size, shape, composition, and surface properties.

Recently, nanotechnology and microfluidics have experienced sustained growth because of the confluence of both fields for drug delivery applications. Microfluidic technology has emerged as a promising alternative process for improving the properties of nanocarriers, including uniformity, complex shape, controlling size, and encapsulation/loading efficiency [25,26]. Microfluidic technology has attracted such vast interest because of its unique and versatile advantages over conventional batch processes, including nanoliter volume manipulation, reduced reaction time, and rapid fluid mixing [24]. Recent studies have focused on functional NP formulation and drug encapsulation via nanoprecipitation under fast and elaborate fluid mixing, taking advantage of the excellent performance of microfluidics [27–29].

Unlike in the bulk process, where fluid mixing occurs via turbulent flow, mixing in microfluidic channels is generally accomplished via diffusion due to laminar flow, which is influenced by convective flow. Although diffusion-based mixing is an inherently slow process, it is much faster than bulk mixing because of the short diffusion length of tiny microfluidic channels. Fluid mixing in microfluidics can be classified into two categories: active and passive mixing [30]. Active microfluidic mixers are achieved by integrating externally applied fields (such as electric, magnetic, acoustic, and thermal) that can generate fluid oscillation and microvortex [31–35]. Although these mixers can perform fluid mixing extremely faster than passive mixers, their NP production is challenging to scale-up because of the need for external apparatuses and high costs. Thus, active micromixers are particularly suitable for mixing specific samples, such as high-molecular-weight and viscous fluids. Meanwhile, passive microfluidic mixers, based on geometric manipulation of flow, can achieve scalable and high mixing performance without any external actuator [36,37]. A common example of 1D streamline-based passive mixing is hydrodynamic flow-focusing (HFF) in a simple straight microchannel; the HFF depends predominantly on diffusion-based mixing because of the inherent laminar flow at low Reynolds numbers (Re). Although drug-loaded PLGA NPs synthesized using a 1D microfluidic mixer show a smaller size and narrower size distribution compared with those produced using the bulk method, it poses a significant challenge in mixing strategies to overcome the clogging of the channels resulting from NP aggregation on the channel wall and low encapsulation efficiency (<60 %) and drug loading (<10 %). To improve the mixing efficiency even at low Re, researchers have designed specific geometries to generate secondary 2D vortices in a microfluidic mixer, such as serpentine and split-and-recombine microchannels, a herringbone structure, and pillar structures [36,38–40]. In these designs, the mixing efficiency can be improved by generating secondary flow unlike 1D mixing, owing to the increased contact area and interaction time between the two mixing species. However, it still suffers from channel clogging and low drug loading (<10 %) [18,41]. To date, several previous studies have observed that 3D designed microfluidic mixer generate effective vortices and achieve high mixing efficiency [29,42,43]. However, the use of 3D microfluidic mixers for drug encapsulation in NPs has not been well reported. Alternatively, microfluidic-assisted flash nanoprecipitation offers a versatile method for generating 3D coaxial flows and for drug encapsulation, which are critical for turbulent flow-based rapid mixing and preventing channel clogging; however, in this method, there is limited scope for scaling up the production rate via parallelization for single-set fluid operation [44–46]. Thus, it is significantly challenging to design a special 3D structure based on a scalable passive microfluidic mixer to enhance the mixing efficiency for simultaneously achieving high encapsulation efficiency and high drug loading.

An emerging approach in this field is 3D printing, which can improve the performance of passive microfluidic mixers by integrating 3D complex designs. Unlike cleanroom processes, 3D printing ensures the automatic construction of 3D architectures with a computer-aided design (CAD) model, eliminating complex procedures and the need for specialized training [47,48]. Generally, 3D flow can generate stronger convective circulations and vortices than 2D planar mixing. The development of special geometries using 3D printing has resulted in a significantly increased fluid–fluid interface area, which enhances the mixing speed in tiny microchannels that generally support laminal flow [42,49,50]. Among all the several passive micromixers that have been investigated, modified Tesla structures have been found to exhibit excellent mixing performance via the Coanda effect, which can induce transverse dispersion between fluids [51–53]. However, the mixing of fluids in these previously modified Tesla structures is based on two-dimensional (2D) flow, which has limited mixing efficiency.

This study aims to design a 3D-geometry-based passive microfluidic mixer with high mixing efficiency for the production of Cur-PLGA NPs (Fig. 1A) with greater control compared with bulk mixing (Fig. 1B). Our passive mixer is constructed by integrating a 3D-HFF microfluidic device with a modified Tesla structure (Fig. 1(C)). To further enhance the mixing performance, we incorporate 3D geometric obstructions (a triangular prism, a cylinder, and a cone) between the Tesla mixing units (Fig. 1(D)). These 3D microfluidic Tesla mixers can be successfully fabricated using a 3D printer. Simulation and experimental results reveal that the Tesla mixer exhibit stronger chaotic advection and better mixing performance with the 3D cone obstructions than with the 2D and 3D triangular prism and cylinder obstructions. By employing the optimal 3D microfluidic Tesla mixer with the cone obstruction, the size and uniformity of PLGA NP formulations can be controlled by varying the solvent type, polymer concentration/molecular weight, and flow condition. Importantly, this microfluidic method enable the Cur-PLGA NPs to exhibit better encapsulation efficiency (EE) and drug loading (DL) when compared to the conventional bulk method. To validate drug delivery application, in vitro studies are conducted on curcumin release with different degradation rates as the pH changed.

2. Experiments

2.1. Materials

A photocurable resin (PlasClear V2) for 3D printing was purchased from ASIGA. Four types of PLGA polymers (PLGA 50:50, 30–60 kDa; PLGA ester terminated 50:50, 24–38 kDa: PLGA ester terminated 50:50, 38–54 kDa; PLGA ester terminated 50:50, 54–69 kDa; PLGA ester terminated 50:50, 100 kDa), acetonitrile (ACN), acetone, dimethyl sulfoxide, 1,4-dioxane, tetrahydrofuran (THF), ethanol, phosphate-buffered saline (PBS), citric acid, sodium citrate, curcumin, and tween 80 were purchased from Sigma-Aldrich.

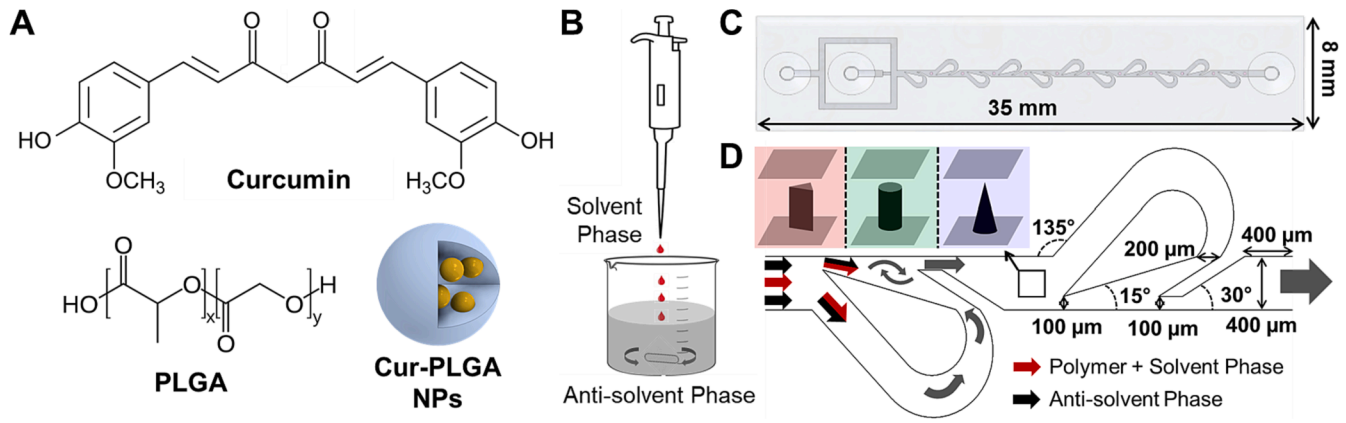

Fig. 1. Microfluidic and bulk methods for producing Cur-PLGA NPs via nanoprecipitation. (A) Chemical structures of curcumin and PLGA and the schematic illustration of the Cur-PLGA NPs. (B) Schematic illustration of the bulk method for producing Cur-PLGA NPs using solvent and antisolvent phases. (C) Schematic illustration of the microfluidic device with 11 Tesla mixers. (D) Detailed Tesla structure with three different 3D obstructions (triangular prism, cylinder, and cone).

2.2. Design and fabrication of the microfluidic mixing device by 3D printing

To directly fabricate the microfluidic mixer, we used a stereolithography and a digital light process (SLA-DLP) 3D printer (MAX X27, ASIGA). First, the microfluidic mixers were designed using Autodesk® Inventor software. The printing part had a total dimension of 35 mm × 8 mm and consisted of two parts: a microfluidic part with a mixing channel (2.0 mm in thickness) and two injection ports as well as one outlet port (3.0 mm in height and 1.0 mm in diameter) (Fig. 1C). Additionally, the design of the microfluidic mixer comprised two parts: a 3D-HFF component (0.5 mm in length, 0.2 mm in width, and 0.2 mm in height) and a Tesla structure mixing channel. For dimensions below 0.2 mm, the microchannel can be blocked during 3D printing. The smallest dimension obtained using the SLA-DLP 3D printer is 200 μm for our optimized printing condition. Fig. 1D shows the detailed Tesla structure. The Tesla mixer part has a height and length of 1.0 mm and 24.3 mm, respectively. There are obstructions along it and upon the bottom surface of the channel with a height of 0.5 mm. Three types of obstructions were designed, namely triangular prism (side length: 0.2 mm), cylinder (diameter: 0.2 mm), and cone (diameter: 0.2 mm), and their mixing performance was compared. For 3D printing of a cone obstruction in a microchannel, the dimensions of the conical structure that can be constructed with the SLA-DLP 3D printer are limited to 0.5 mm for the height and 0.2 mm for the diameter. Next, we converted the 3D CAD file to STL format and set up the UV exposure (wavelength: 385 nm and power: 40 mW/cm^2) on the 3D printer. The exposure time for the initial 10 printed layers was set at 10 s per layer and subsequently reduced to 1.5 s for the remaining printed layers. After the 3D printing process, the printed devices were removed from the constructed platform, washed with ethanol, and dried. Finally, we post-cured printed device for 20 min in the ASIGA Flash (ASIGA).

2.3. Computational fluid dynamics (CFD) simulation

The microfluidic mixers were designed using the CAD software Autodesk® Inventor. Thereafter, to simulate the fluid-flow profile in the microchannel, mixer models were exported and meshed in COMSOL Multiphysics 6.0 using a laminar flow module with 3D models. The operating fluid was water with a specific density of 999 kg/m^3 and a dynamic viscosity of 8.8 × 10^{-4} kg/(m·s) at 293.15 K. The assumed equations for the analyses of flow velocity are as follows:

Conservation of mass:

$$\nabla.\left(\rho\vec{V}\right) = 0 \tag{1}$$

Navier–Stokes equation:

$$\rho(\mathrm{u}.\nabla).\mathrm{u} = \nabla.[-pI + K] + F \tag{2}$$

where ρ, *V*, u, *p*, K, and F are the fluid density, fluid velocity, flow velocity vector field, pressure, viscous stress tensor, and surface tension force, respectively.

A steady-state flow regime was assumed during the numerical solution of the governing equations. Uniform velocity profiles were imposed at the inlets with a total fluid flow rate of 50 mL/h, which is similar to the experimental parameters for microfluidic mixing. The outlet was assigned a static pressure of zero, whereas the wall condition was specified as a no-slip boundary condition.

2.4. Evaluation of mixing performance

To analyze the mixing performance, we injected deionized (DI) water and 0.05 mg/mL of fluorescein sodium salt into the device via a polyethylene tube using syringe pumps (Standard PHD ULTRA™ CP, Harvard Apparatus). Flow rates of 45 mL/h and 5 mL/h were used for the DI water and dye solution, respectively. The fluorescence was monitored using an inverted microscope (Eclipse Ti2-U, Nikon Instruments Inc.) with a digital camera (DS-Qi2, Nikon Instruments Inc.) supported by NIS-Elements AR software, and then it was analyzed using ImageJ software (ImageJ, NIH). The mixing index was calculated using Eq. (3) based on changes in the coefficient of variation (CV) of the gray value in a defined area.

$$\text{Mixing index} = \left(1 - \frac{\mathrm{CV}_1}{\mathrm{CV}_2}\right) \times 100\% \tag{3}$$

where CV_1 is the CV of the gray value measured when two inlets are filled with water as the continuous phase and a dye solution as the disperse phase, and CV_2 is the CV of the gray value measured when both inlets are filled with the dye solution. This was considered a state of complete mixing and used for the control samples.

2.5. Formulation of polymeric NPs

PLGA NPs were prepared using both the bulk method and the microfluidic mixer (Fig. 1B and C). We prepared an antisolvent phase comprising 1 mg/mL of tween 80 in DI water and a solvent phase comprising PLGA or a PLGA and curcumin mixture dissolved in ACN. All solutions were filtered through a 0.22 μm pore filter (Advantec®, Tokyo Roshi Kaisha) to eliminate contaminants. For NP formulation using the bulk method, the solvent-phase solution containing PLGA (2 mL) was directly dropped onto the antisolvent solution (20 mL) under stirring for

1 min. The mixture solution was stirred overnight. For the microfluidic formulation, the two solutions were injected through the inlets at various flow rates, and then the NP suspension was collected in the tube. To control the PLGA NP formulation, we varied the experimental conditions, including the solvent type, PLGA concentration, PLGA molecular weight, flow rate ratio, and total flow rate. Experiments were conducted to evaluate the effects of the solvent types, PLGA concentration, and PLGA molecular weight, with the flow rates of the antisolvent and solvent phases set at 80 mL/h and 32 mL/h, respectively. Meanwhile, to examine the impacts of the flow rate ratio and total flow rate, we varied the flow rates of the two phases using 2.5 mg/mL of the 24–38 kDa PLGA solution as the solvent phase and D.I. water as the antisolvent phase. The NP solutions produced using the bulk and microfluidic methods were centrifuged (12500 rpm, 12 min) three times using a microcentrifuge (Smart 13, Hanil Scientific Inc.) to remove any residual chemicals and organic solvent. The sedimented particles were dried completely under a vacuum at room temperature.

2.6. Characterization of the hydrodynamic size and morphology

A zeta-potential and particle-size analyzer (ELSZ-2000, Otsuka Electronics) was used for dynamic light scattering (DLS) measurements to determine the hydrodynamic diameter and polydispersity index (PDI) of the NPs. SEM images were obtained using a field-emission scanning electron microscope (Sigma 500 VP, Zeiss) at 5 kV.

2.7. Characterization of the EE and DL of the Cur-PLGA NPs

The EE and DL of the Cur-PLGA NPs were evaluated using a UV–Vis spectrophotometer (Ubi-490, MicroDigital Co., Ltd.) at 420 nm absorbance. Briefly, a calibration curve was obtained using different curcumin concentrations of 0.001–0.050 mg/mL in ACN. The Cur-PLGA NPs were washed with DI water or ethanol, and then 1.5 mg of the Cur-PLGA NPs were dissolved in ACN to completely release curcumin. Next, the absorbance of this solution was measured at 420 nm to determine the amount of released curcumin.

$$\text{EE } (\%) = \frac{\text{curcumin amount in NPs}}{\text{initial curcumin amount}} \times 100\% \quad (4)$$

$$\text{DL } (\%) = \frac{\text{curcumin amount in NPs}}{\text{mass of NPs}} \times 100\% \quad (5)$$

2.8. In vitro curcumin release and stability study

To determine the kinetics of the release of curcumin from the PLGA NPs, 1.0 mg of the Cur-PLGA NPs were redispersed in 10 mL of PBS buffer (pH 7.2) or citric acid buffer (pH 5.5), and then the suspensions were incubated in an incubated shaker (IST-3075, JeioTech) at 100 rpm and 37 °C. The Cur-PLGA NP solution was periodically collected and centrifuged at 12500 rpm for 12 min. The supernatant was measured using the UV–Vis spectrophotometer to determine the amount of released curcumin. The stability of the Cur-PLGA NPs was carried out in PBS buffer (pH 7.2) within 7 days at 25 °C. The NPs solution was sealed in glass vials, samples were withdrawn at different intervals (1, 3, 5, and 7 days), and the z-average size and polydispersity index (PDI) were analyzed via dynamic light scattering (DLS).

3. Results and discussion

3.1. Microfluidic mixer design and numerical modeling

As shown in Fig. 1C, the microfluidic mixing device comprises a 3D-HFF cross-junction and eleven repeating Tesla mixing units for mixing purposes. Fig. 1D shows details of our geometric consideration for the Tesla structure with three types of 3D obstructions. The fluid stream with the polymer solvent phase centered inside the antisolvent phase is introduced into the Tesla mixers through 3D-HFF. The edge sharp structure splits this fluid stream into two sub-streams. One sub-stream is strongly squeezed and directed to combine with the transverse direction flow of another side fluid stream, which can enhance micromixing due to the increased inertia effect that occurs after a strong collision between the fluid streams with different flow rates. Additionally, the Tesla structure exhibits the Coanda effect, which is the tendency for fluid to flow along a curved surface rather than a straight line, which can enhance mixing performance by introducing chaotic advection [54]. We expect that fluid flow can behave very differently when 3D obstructions, including triangular prism, cylinder, and cone, are incorporated into a Tesla mixer.

To confirm our hypothesis, we use COMSOL multi-physics to numerically investigate the flow behavior of the incompressible solution by solving the continuity and Navier–Stokes equations and the convection–diffusion equations. The velocity vectors for six distinct Tesla mixers with 2D planar and incorporated 2D and 3D obstructions are shown on the *x*–*y* and *x*–*z* planes (Fig. 2). The 2D obstructions have the same height as the channel, and the 3D obstructions have a lower height than the channel, affecting fluid flow in three dimensions. We observe nearly horizontal streamlines along the channel length in the reference 2D planar Tesla mixer (Fig. 2A), but no secondary flow, such as vortical flow, is observed. Contrarily, vortical flows are frequently generated in front and behind the obstructions in the other Tesla mixers with 2D (Fig. 2B and D) and 3D (Fig. 2C, E, and F) obstructions. Additionally, when compared to the 2D planar Tesla mixer, the Tesla mixers with obstructions have a higher difference in flow rate between the two sub-streams at the joint where the sub-streams from the squeezed and curved channels collide. This is because of the presence of obstructions. The fluid stream unevenly splits into two streams because of the different flow resistances between the squeezed and curved directional channels [55]. The curved channel has relatively high flow resistance due to its long channel length. Meanwhile, for the Tesla mixers with obstructions, the obstruction tends to induce additional fluid flow to the curved channel, which can increase the residence time for enhanced mixing, unlike the 2D planar Tesla mixer. We observe that the 3D obstructions induce stronger vortical flows than the 2D obstructions for both the triangular prism and cylinder shapes (Fig. 2B–E). Although the vortical flow in the wake region behind the obstruction is minimized, the flow streamlines are generally well dispersed in the Tesla mixing channel, even onto the 3D obstructions (on the *x*–*y* plane, Fig. 2B–E). Additionally, the vortical flows generated in front of the 3D obstructions are stronger than those generated in the 2D obstructions (Fig. 2C and E). These 3D obstructions can induce significant deformations in the flow stream around the surface wall of the obstruction and the gap between the roof of the obstruction and the ceiling wall of the channel, which may contribute to efficient mixing performance (on the *x*–*z* plane, Fig. 2C and E).

The interesting 3D geometry is a conical structure with different curved surfaces that taper smoothly from a flat circle base to a single point. As shown in Fig. 2F, the Tesla mixer with a 3D cone obstruction has denser streamlines at the vortical flow region than the Tesla mixers with triangular prism and cylinder obstructions. Conversely, no secondary vortical flows are observed in front of both the 2D and 3D obstructions when a simple straight channel is used, unlike in the case of the Tesla mixer channel (Fig. S1). We predict that the main causes of the strong vortical flow at the 3D cone obstruction in the Tesla mixer are as follows: (1) When the fluid approaches the cone obstruction, the hydrodynamic pressure increases owing to the narrowing of the space between the microchannel and obstruction. Such hydrodynamic pressure is uneven near the conical structure because the narrowing space gradually changes depending on the tapered circle diameter. This indicates that under laminar flow in the microchannel, large differences in shear force between fluid layers from uneven flows induce significant deformations in fluid flow, possibly generating rotational secondary

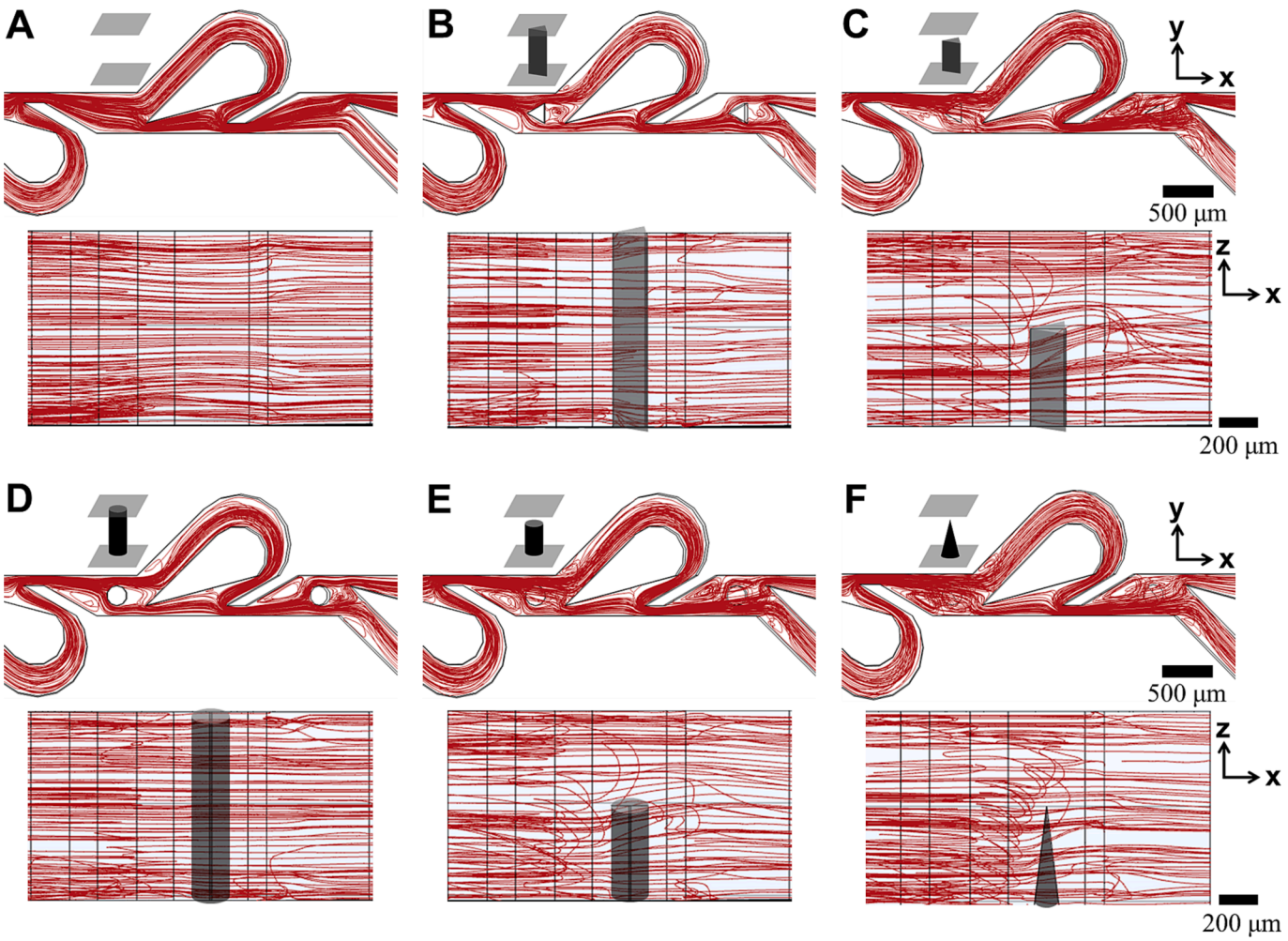

Fig. 2. Flow streamlines obtained from the 2D velocity profile simulation (*x*–*y* and *x*–*z* planes) for six different Tesla mixers: (A) 2D planar Tesla mixer, Tesla mixers with (B) 2D triangular prism, (C) 3D triangular prism, (D) 2D cylinder, (E) 3D cylinder, and (F) 3D cone obstructions.

flows. (2) The squeezed fluid flow in the Tesla structure expands in front of the obstruction, thereby inducing variations in velocity and pressure [56]. Such dynamic fluid flow behavior caused by the special structure provides a unique opportunity to use the driving force for better mixing performance when compared to using a simple straight channel.

3.2. *Mixing performance of the 3D-obstruction-integrated microfluidic Tesla mixer*

As briefly discussed above, the 3D obstruction existing under fluid flow can enhance the mixing performance; thus, we attempt to fabricate a microfluidic mixer by incorporating the three obstructions between the Tesla mixing units to validate numerical simulation results. The 3D printing method can be used as an alternative method to fabricate a master mold template for the soft lithography of a microfluidic device. In particular, the SLA-DLP 3D printing method is a suitable candidate for the production of microfluidic devices with fine channels [48,57,58]. With the evolution of the 3D printing resolution, there is a compelling need for a 3D-printer-based simplified manufacturing process for the direct fabrication of entire microfluidic devices. We use SLA-DLP 3D printing to directly form 3D-HFF and complex 3D structures, including a triangular prism, a cylinder, and cone shapes. The layered structures can be clearly observed in all the SEM images, indicating that the 3D printing process constructed the material layer by layer (Fig. S2A-C). We determine the surface roughness of the layered structure of the sidewall of the 3D printed device. The surface roughness was calculated to be 13.87 μm from the equation presented in Fig. S2D [59]. The surface roughness of these layered structures increase, thereby decreasing the flow velocity onto the surface and causing flow instability, which may have enhanced the mixing performance [60,61]. Although the 3D printing process has limited ability to form cone structures with a low resolution, the key shape for the tapered circle diameter is still present (Fig. S2C).

To examine the impact of various impediments on mixing performance, we use the green fluorescent dye to visualize the fluid mixing streams and then quantify a mixing index for different mixing units: a 1D straight microchannel, the 2D planar Tesla mixer, the Tesla mixer with 2D obstructions, and the Tesla mixer with 3D obstructions. Fig. S3A illustrates fluid mixing in the Tesla mixers with 2D triangular prism and 2D cylinder obstructions. Narrow center streams are observed at the 3D-HFF junction channel, where the two injected fluids meet. This fluid stream to be mixed flows dependently along the mixing channel geometry. Since the obstructions are 2D, no fluorescence is observed at their position, but fluid streams with different fluorescence intensities are clearly observed around them. Fig. 3A shows the fluorescence observation results for fluid mixing in the 2D planar Tesla mixer and the 3D-obstruction-integrated Tesla mixer. Generally, fluorescence molecules continually diffuse out as the number of units increases, indicating that mixing is occurring. Compared to the case of the 2D planar Tesla mixer, different flow patterns are visualized around each obstruction in the Tesla mixer with 2D and 3D obstructions, implying that Tesla mixers with obstructions are more feasible for generating additional secondary

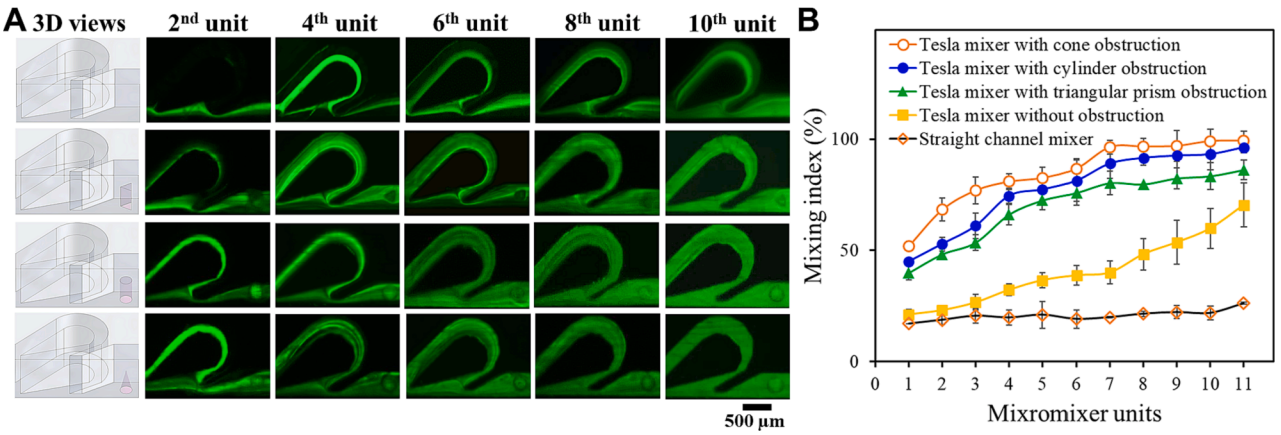

Fig. 3. Mixing characterization of various types of microfluidic Tesla mixers. (A) Schematic illustration of 3D views and fluorescence images of fluid mixing for the reference 2D planar Tesla mixer and the three 3D Tesla mixers with triangular prism, cylinder, and cone obstructions. The fluorescence images are captured at different units along the Tesla mixing channel. The flow rates of the injected fluorescence and blank solutions are 5 and 45 mL/h, respectively. (B) Quantification of mixing versus mixing units for five different geometries. The mixing index is obtained by measuring the coefficient of variation (CV) of the fluorescence intensity in a defined area at the exit of each Tesla mixing unit. Data represent the mean (±SD) of five independent experiments.

flow mixing than Tesla mixers with no obstructions (Fig. 3A and S3A). Specifically, very weak fluorescence is present at the curved channel of the initial mixing unit (second unit) in the 2D planar Tesla mixer because the main flow is in the direction of the squeezed channel owing to low resistance. In contrast, relatively high fluorescence intensities is present at the curved channel in the 3D-obstruction-integrated Tesla mixers because the obstruction cause the main fluid stream to slightly shift to the direction of the curved channel. This phenomenon is consistent with the simulation results, which reveal remarkable differences in velocity between the squeezed and curved channel flow streamlines at the joining region (Fig. 2).

The quantitative mixing index indicates significantly different mixing behaviors depending on the mixing geometries (Fig. 3B and S3B). Specifically, a mixing index of 100 % indicates complete mixing of the blank and fluorescence solutions. Mixing in the straight channel relies only on diffusion due to the absence of secondary flow, resulting in a low increase in the mixing index from 17.0 % to 26.2 % along the 23.9 mm channel length (Fig. 3B). Compared to the 1D straight channel, the 2D planar Tesla mixer significantly improve fluid mixing from 21.2 % to 70.4 %. This can be achieved through three approaches related to channel geometry: (i) the appearance of a flow plate, which suddenly reduces the width of the exit channel and intensifies the contact between the two rejoined fluid streams; (ii) the centrifugal forces generated in the curved channels, which cause the fluids to produce secondary flows; and (iii) the split-and-recombine structure of the flow channels, which lessens the diffusion distance between the two fluid streams [62,63]. As expected, the simulation results reveal that the Tesla mixers with 3D obstructions have higher mixing index values than the 2D planar Tesla mixer for all cases of obstructions, increasing to 86.2 % (triangular prism), 96.3 % (cylinder), and 99.4 % (cone) (Fig. 2B). The cone obstruction has a higher mixing index of $>$ 95 % at the 7th unit than the cylinder obstruction, which has a mixing index of 96.3 % at the 11th unit. The cone obstruction achieve complete mixing within 400 ms at a flow rate of 50 mL/h. Our results demonstrate that the geometric characteristics of an obstruction would affect transverse flow formation in a Tesla mixer. Cylinder obstructions have a curved surface that can form stronger Dean vortices than triangular prism obstructions, thereby leading to a stronger transverse flow and a higher mixing index [53,64]. Similarly, the Tesla mixer with the cone obstruction has a higher mixing index than that with the cylinder obstruction. Conical structures mainly differ from cylinder structures in that they have asymmetric curved surfaces. We believe that such asymmetric cone structures would result in deformed transverse flow as their diameters gradually change, which can be attributed to the gradual deformation of the inertial flow stream around the cone surface. Fig. S3B compares the mixing indexes for the 2D and 3D obstructions. The 3D obstructions have significantly higher mixing indexes at the 11th unit than the 2D obstructions, indicating that 3D geometry exploits vortical mixing to improve the performance of microfluidic mixers. This supports the hypothesis that the geometry of obstructions plays a critical role in determining the mixing efficiency of 3D-printed microfluidic mixers.

3.3. *Controlled formulation of PLGA NPs using the 3D microfluidic Tesla mixer*

We formulate drug carriers using microfluidic mixers in order to create controlled polymeric NPs with uniform sizes, which are important parameters for controlling drug release kinetics. As previously mentioned, the 3D microfluidic Tesla mixing process is designed to achieve rapid mixing, which is advantageous for formulating NPs with small diameters and narrow size distributions. In addition to mixing design, microfluidic HFF junctions where two solutions converge play a critical role in determining the size and distribution of NPs. To investigate the differences in NP formulation according to the HFF junction design, we use a 3D-printed microfluidic device comprising the 3D-cone-obstruction-integrated Tesla mixer as the mixing component and a 2D-HFF or 3D-HFF geometry as the junction component. Upon comparing the PLGA NP formulations, largely aggregated polymers are observed at the solvent–antisolvent interface in only the 2D-HFF junction (Fig. S4A). This aggregation occur because of liquid–liquid interface contact onto the channel surface; in contrast, such an interface in the 3D-HFF junction is formed inside the channel, preventing aggregation[65–67]. To quantitatively compare this difference, we measure the change in the *z*-average size and PDI of the PLGA NPs with operating time (Fig. S4C). The sizes of the NPs synthesized in the 2D-HFF and 3D-HFF junctions are in the ranges of 90–110 nm and 101–105 nm, respectively. The PDIs of the NPs are in the ranges of 0.11–0.16 (2D-HFF) and 0.08–0.10 (3D-HFF). Using the 3D-HFF microfluidic Tesla mixer, we also evaluate the effect of the obstructing structure on PLGA NP formation (Fig. S4D). The different obstructing structures are found to correspond to different mixing efficiencies. The size and PDI of PLGA NPs produced in the Tesla mixers with a 3D triangular prism obstruction (131.67 nm size and 0.12 PDI) and a 3D cylindrical obstruction (106.63 nm size and 0.11 PDI) are greater than those of NPs produced in the Tesla mixer with a conical obstruction (98.0 nm size and 0.07 PDI). This trend further strengthens our hypothesis that the mixing ability of the Tesla mixer design is directly related to the size and uniformity of the PLGA particles produced. Through an appropriate choice of the obstruction shape, the

mixing ability of the mixer can be improved. This would facilitate the production of PLGA NPs with controlled properties. Additionally, there are no variations in size or PDI values among the devices (Fig. S4D). Thus, we can confirm that the 3D-printed microfluidic mixer with 3D-HFF enables the reproducible formation of PLGA NPs with homogeneous size distributions.

The basic principle of polymeric NP formulation is nano-precipitation, which occurs when the solution changes its polarity after being diluted with a polymer-containing organic solvent in an aqueous solution. Two main factors affect the size and uniformity of NPs: change rate and difference in polarity between the antisolvent and solvent. To evaluate the controllability of the NP size based on these factors, we formulate the PLGA NPs with four organic solvents and DI water as the antisolvent using both our 3D microfluidic Tesla mixer and the bulk method. Our microfluidic mixer exhibit enhanced mixing performance, which is closely related to polarity change rate. As shown in Fig. 4A, the 3D microfluidic method produce smaller PLGA NP sizes and lower PDI values than the bulk method in all cases of organic solvent. Furthermore, the organic solvents used have a significant influence on both the size and PDI of the PLGA NPs. The polarity indexes of 1,4-dioxane, THF, acetone, and ACN are 0.164, 0.207, 0.355, and 0.460, which are lower than the polarity index of water (1.000) [68]. Since the polarity index of the solvent phase is close to that of water, the formulated NPs are small and uniform: 196.3 nm size and a 0.14 PDI in 1,4-dioxane, 173.3 nm size and a 0.12 PDI in THF, 127.1 nm size and a 0.07 PDI in acetone, and 98.0 nm size and a 0.07 PDI in ACN. SEM images show that PLGA NPs formed with four different solvents by our microfluidic mixer have smaller and uniform size morphologies compared to bulk method (Fig. S5). The high performance of our microfluidic mixer and the high polar index of ACN indicate excellent diffusion efficiency in the aqueous water phase, which affects the homogeneity of the nucleation step as well as the diameter and uniformity of the precipitated NPs.

Next, we evaluate the effect of the PLGA concentration on the size and uniformity of the NPs in our 3D microfluidic Tesla mixer. As the PLGA concentration increased, the NP size and PDI steadily increase from 98 nm and 0.076 to 138.9 nm and 0.16, respectively (Fig. 4B). It is well known that high polymer concentrations increase the viscosity of the solution and decrease the distance between polymers, leading to increased NP sizes due to a decrease in the diffusion and mixing rates [69,70]. Meanwhile, both solution viscosity and polymer solubility vary as PLGA molecular weight changes, which can inversely affect NP formulation [71,72]. Specifically, the solution viscosity increase as the molecular weight increased, resulting in increased NP sizes, as previously mentioned. In contrast, solubility decrease as the molecular weight increased, resulting in decreased NP sizes owing to rapid precipitation. However, our results reveal no significant changes in the size and PDI of the PLGA NPs formulated using the four PLGA molecular weights (79.2–94.2 nm sizes and 0.076–0.12 PDIs) (Fig. 4C). As the PLGA molecular weight decrease, the PDI values slightly decrease, but average size of the PLGA NPs do not show a definitive trend. We expect that the high mixing rate of our device can improve the mobility of high-molecular-weight polymers, which may minimize the effect of molecular weight on NP formulation relative to the polymer concentration effect.

To further investigate the influence of the flow condition in the 3D microfluidic Tesla mixer, we compare the size and PDI of the formulated PLGA NPs by varying the total flow rate and flow rate ratio ($Q_{sol}/Q_{antisol}$) of the solvent and antisolvent solutions. As shown in Fig. 4D, the NP size decrease as the total flow rate increased, which is due to improved the mixing performance, but it moderately increase as the flow rate ratio increased. The dependence of mixing performance on total flow rate has been discussed in previous reports [73,74]. Furthermore, changes in the flow rate ratio can affect NP formulation by changing the polarity of the antisolvent and solvent mixture, as the NP size depends on the polarity

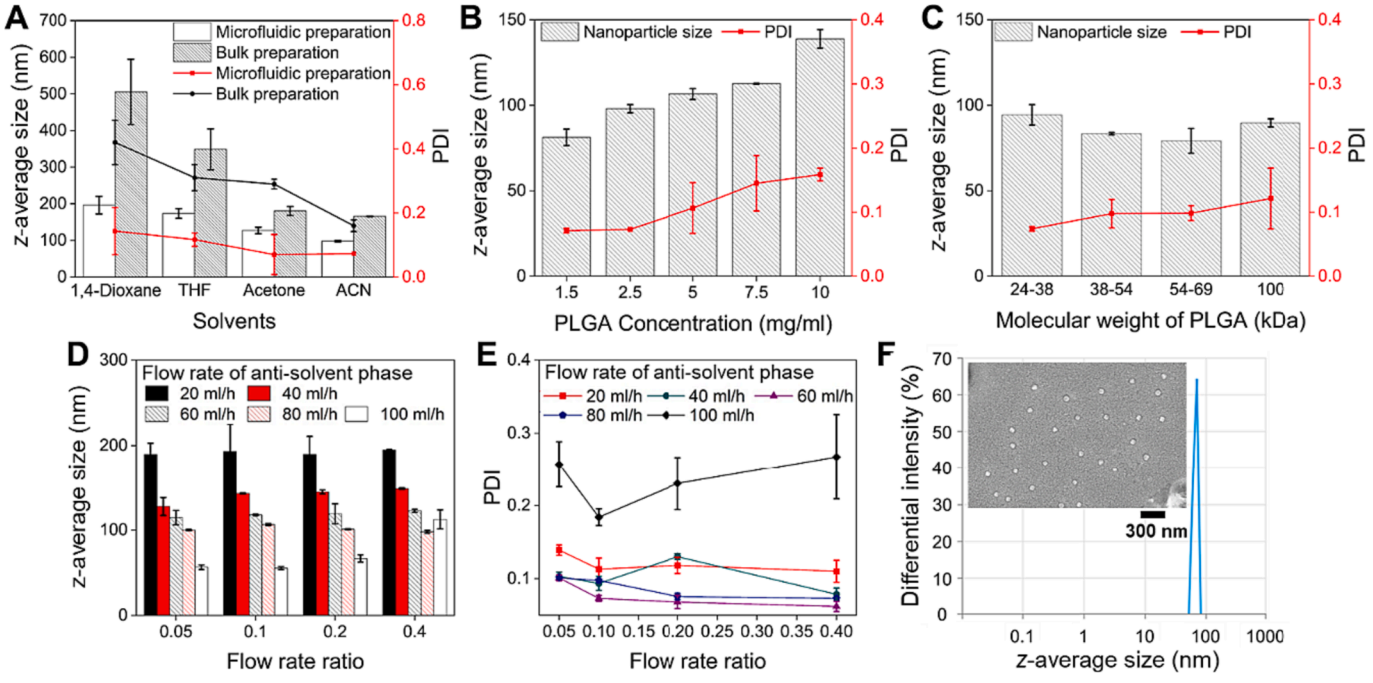

Fig. 4. Controlled formulation of PLGA NPs using 3D microfluidic Tesla mixer. An aqueous antisolvent phase containing 1.0 mg/mL of Tween 80 and an solvent phase containing PLGA are used. (A) Comparison of the bulk and microfluidic methods for PLGA NP formulation and the effect of four solvents on the *z*-average size and PDI value; the four solvents were 1,4-dioxane, tetrahydrofuran (THF), acetone, and acetonitrile (ACN), with all of them containing 2.5 mg/mL PLGA. (B) Effect of the PLGA concentration (1.5–10 mg/mL PLGA in ACN) on the *z*-average size and PDI value. (C) Effect of PLGA's molecular weight on the *z*-average size and PDI value (2.5 mg/mL PLGA with a molecular weight in the range of 24–100 kDa in ACN). (D, E) Effect of the total flow rate and flow rate ratio between solvent and antisolvent phases on the *z*-average size and PDI value (2.5 mg/mL PLGA (24–38 kDa)). (F) DLS analysis and an SEM image of the optimized formulation of small and uniform PLGA NPs (2.5 mg/mL PLGA (24–38 kDa) in ACN is used as the solvent). A total flow rate of 112 mL/h and a flow rate ratio of 0.4 are used in the 3D Tesla mixer. Data represent the mean value (±SD) of five independent experiments.

of the mixture [75]. It has also been reported that the influences of flow conditions on the NP size depend on the polymer type [74,76,77]. However, in this study, the NP size is not influenced by changes in the flow rate ratio at a total flow rate of 20 mL/h. The fluid injected for 3D-HFF divide into two uneven streams at the entrance of the Tesla structure, indicating that the solvent/antisolvent ratio is uneven. The low solvent ratio existing in the middle flow of 3D-HFF may have leaned to one side path, which can induce NP nucleation in a concentrated antisolvent mixture before complete mixing occurs. Although the flow rate ratio increase, the nucleation condition may not have changed significantly in the Tesla structure with two paths, resulting in no significant variation in the PLGA NP size. At a high total flow rate of 100 mL/h, the NP size increase owing to improved mixing performance, which minimize the mixing variation between the two paths in the Tesla structure. Fig. 4E shows that the flow conditions influence the size distribution of the NPs. The total flow rate of 20 mL/h cause relatively low mixing performance, resulting in a wide size distribution. Although increasing the total flow rate induces high mixing performance, the total flow rate of 100 mL/h cause a wide NP size distribution because the fluid residence time in the microfluidic mixer is very short and broadly distributed [74,78]. We find that PLGA NPs with low PDI values are obtained at flow rates of 40–80 mL/h in most flow rate ratios. On the basis of the results of the validation of the method for controlled NP production, we produce small and uniform PLGA NPs with a *z*-average size of 81.3 nm and a PDI of 0.071 by using the 3D microfluidic Tesla mixer (Fig. 4F). For comparison, the SEM images show the spherical morphology of NPs with a size of 77.2 ± 6.93 nm, which are slightly smaller than the DLS measurements (*z*-average size of 81.3 nm) owing to the effect of the hydrodynamic diameter in an aqueous environment.

3.4. *Exceptional drug encapsulation in the 3D microfluidic Tesla mixer*

One of the major challenges in the drug application of polymeric NPs is achieving high encapsulation of water-insoluble drugs to attain high drug efficacy. We believe that nanoprecipitation can occur through the coprecipitation of drug molecules and polymer and through the precipitation of drug molecules with one another, which can affect the EE and DL. Nonencapsulated curcumin can aggregate into crystalline nanostructures, which do not easily dissolve in body fluids, causing low drug efficacy [79]. To overcome these challenges, we design 3D microfluidic Tesla mixers to enhance encapsulation performance. We characterize the Cur-PLGA NPs formulated using three different preparation methods, namely, bulk mixing, microfluidic straight mixing, and 3D Tesla mixing, to compare the drug encapsulation performance (Fig. 5). Fig. 5A shows that the co-precipitated Cur-PLGA NPs produced in the 3D Tesla mixer had larger sizes and PDI values (93.33 nm and 0.073, respectively) than the bare PLGA NPs (81.25 nm size and 0.071 PDI). The Cur-PLGA NPs with the largest sizes and PDI values are produced by the straight microfluidic mixer (182.6 nm size and 0.14 PDI) and bulk mixer (380.8 nm size and 0.34 PDI). These trends are clearly due to the superior mixing ability of the 3D Tesla mixer when compared to those of the straight and bulk mixers.

To further evaluate the drug encapsulation ability of the 3D Tesla mixer, we prepare Cur-PLGA NPs using the microfluidic mixer and bulk mixer and then compare the EE and DL of the Cur-PLGA NPs after washing them with DI water (curcumin-insoluble) or ethanol (curcumin-soluble) (Fig. 5B and C). Ethanol was chosen as the washing solvent alternative to DI water to remove the nonencapsulated curcumin particles because it has good curcumin solubility and PLGA miscibility. Compared to DI water washing, ethanol washing slightly reduced the EE and DL for all mixing methods tested: EE decrease from 30.25 % to 10.91 % and DL decrease from 19.46 % to 7.01 % in the bulk mixer, EE decrease from 36.86 % to 32.78 % and DL decrease from 27.41 % to 22.07 % in the straight mixer, and EE decrease from 73.37 % to 68.40 % and DL decrease from 48.27 % to 43.01 % in the 3D Tesla mixer. Interestingly, when the washing solution is changed from DI water to ethanol, both the EE and DL dramatically reduced by more than half in bulk mixing when compared to microfluidic mixing. This demonstrates that nonencapsulated curcumin exists as particles that is difficult to remove via centrifugation and that ethanol is effective for removing

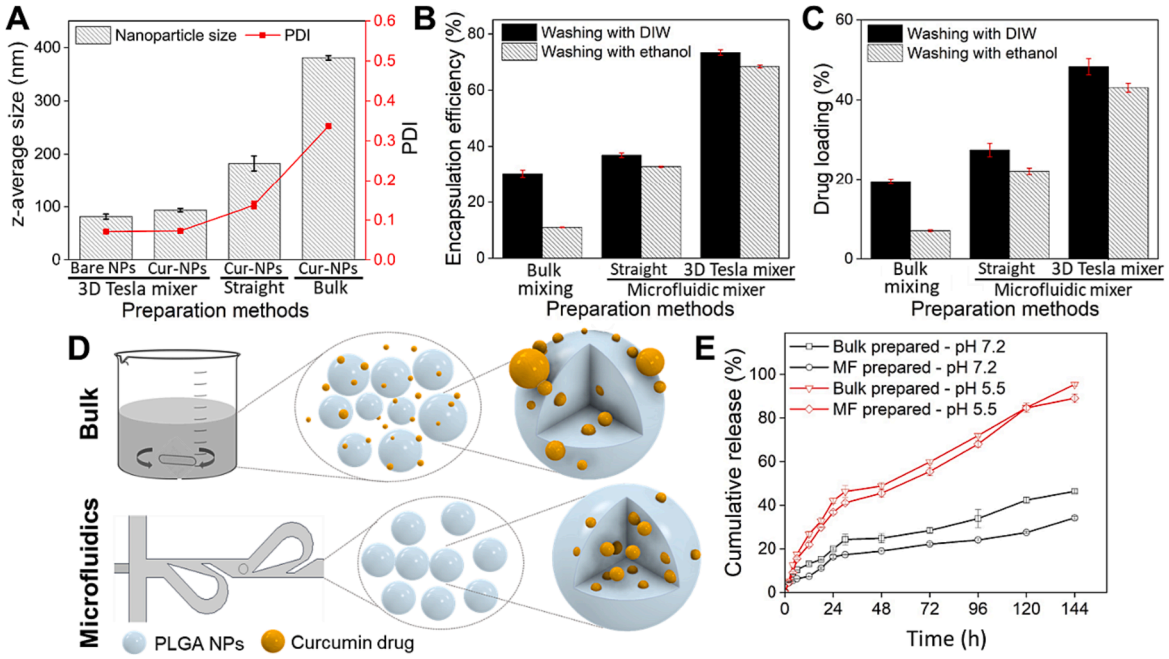

Fig. 5. Comparison of Cur-PLGA NPs produced via microfluidic mixing and bulk mixing. (A–C) Comparison of bulk mixing, microfluidic straight mixing, and 3D microfluidic Tesla mixing methods for encapsulating curcumin in PLGA NPs. (A) Variation in the *z*-average size and PDI of the PLGA NPs and Cur-PLGA NPs. Comparison of the (B) encapsulation efficiency and (C) drug loading between Cur-PLGA NPs washed with DI water and those washed with ethanol. (D) A schematic of the bulk and microfluidic methods for formulating Cur-PLGA NPs. (E) Cumulative release of curcumin from PLGA NPs in pH 7.2 and pH 5.5 environments. The Cur-PLGA NPs are prepared using the 3D microfluidic Tesla mixer (MF) and bulk mixing. Data represent the mean values (±SD) of five independent experiments.

residual curcumin. Evaluating the EE and DL as well as the size and size distribution after washing with DI water can produce false positive results. Importantly, the 3D microfluidic Tesla mixer improve the EE and DL of the PLGA NPs up to six times more than the bulk mixer. Fig. 5D compares the Cur-PLGA NPs formulated using bulk and microfluidic mixing. The low mixing rate of bulk mixing result in reduced frequent interactions between PLGA and curcumin, which lead to increased curcumin aggregation and decreased encapsulation effects. In an aqueous environment, separately formed curcumin particles can adhere to the PLGA NP surface via attractive interaction (van der Waals interactions, hydrophobic interactions, etc.), and they can sediment with the PLGA NPs during centrifugation in the washing process [80]. Notably, we demonstrate that the high mixing rate of our 3D microfluidic Tesla mixer induces continuous interactions between PLGA and curcumin, resulting in high DL. The high DL of the NPs is critical for future clinical applications. Regarding cell-targeted drug delivery, the efficiency of NP delivery highly depends on cellular affinity and ligand density [81,82]. The exceptional drug-loaded NPs can be used to enhance the drug's response to stimuli even with very low targeting moieties. Improving EE for drug carrier nanoparticles is essential for minimizing expensive drug waste during nanoprecipitation. Several studies have demonstrated that EE and DL can vary depending on the encapsulating polymer and drug, as they rely on the intermolecular interaction between the polymer and drug. Therefore, higher encapsulation can be achieved by utilizing novel polymer-carriers with strong drug-carrier interactions under microfluidic mixing [83]. Alternatively, microfluidic nanoprecipitation via co-loading using drug-polymer conjugate and pre-loading using drug nanoparticles could improve EE and DL [84].

Next, we evaluate the release profile of the Cur-PLGA NPs while considering that the surrounding environment of NPs during cellular uptake changes from neutral pH 7.4 in blood to acidic pH 5.5 in endosomes [85]. As shown in Fig. 5E, the Cur-PLGA NPs exhibit a sustained curcumin release profile for 6 days, and the release profile is higher in the pH 5.5 buffer (89.1 % ± 2.0 %) than in the pH 7.4 buffer (34.2 % ± 0.7 %). This difference in curcumin release as the pH changes indicates that PLGA exhibits acid-triggered release behavior due to its rapid degradation [86,87]. In addition, water molecules can penetrate the polymeric network. The curcumin dissolves in the penetrated water, and its release occurs through diffusion. Low pH induces weak interaction between PLGA and curcumin, which results in a slight increase in the solubility of curcumin in water [41,88]. From the results of Cur-PLGA NPs stability (Fig. S6), no significant *z*-average size and PDI changes are observed for 7 days, indicating that drug release in pH 7.4 is predominantly induced by water uptake and swelling of NPs rather than PLGA degradation.

4. Conclusion

This study presents a 3D microfluidic Tesla mixer with high mixing performance for improving the encapsulation of curcumin drugs in PLGA NPs. The microfluidic Tesla mixer with complex 3D geometries, including 3D-HFF and 3D obstructions, is successfully fabricated via 3D printing. We demonstrate that the integration of 3D obstructions into Tesla structures can improve mixing performance by generating additional vortical flows, which is confirmed through CFD simulations. Among the various 2D and 3D obstructions tested, the 3D cone obstruction in the Tesla mixer is found to achieve rapid full mixing within 400 ms. This device allow for the controlled formulation of PLGA NPs with sizes of 79.2–196.3 nm and a PDI value of < 0.1 while varying the nanoprecipitation experimental conditions, including solvent type, PLGA concentration, PLGA molecular weight, total flow rate, and flow rate ratio. Additionally, small and uniform Cur-PLGA NPs are successfully produced using our device. Most importantly, we find that washing the Cur-PLGA NPs with ethanol is critical for purifying them and enabling our 3D microfluidic Tesla mixer to achieve considerably higher EE (68.40 %) and DL (43.01 %) than bulk mixers. Additionally, we demonstrate that the pH-triggered release of Cur-PLGA NPs is feasible for future clinical applications. Our current investigation mainly focuses on improving mixing performance, which significantly affects the quality of drug nanocarriers. It is a promising approach for efficiently encapsulating curcumin, which has shown low EE and DL in previous reports. We expect to achieve higher EE and DL with other drugs using our device. Further investigations of encapsulating other drugs that are approved by the Food and Drug Administration (FDA), such as docetaxel and paclitaxel, are required for the versatility and robustness of our 3D microfluidic Tesla mixer. In addition, with increasing interest in the scaling up of the production of microfluidic NPs, our design is expected to facilitate scalable NP production if the 3D microfluidic Tesla mixer can be (1) fabricated through parallel printing and (2) integrated with the distribution network [36,89]. We believe that the proposed 3D microfluidic Tesla mixer could be widely extended to drug encapsulation and drug delivery applications.

CRediT authorship contribution statement

Phuong Thao Le: Conceptualization, Data curation, Investigation, Methodology, Validation, Writing – original draft. **Seung Hui An:** Investigation, Validation, Writing – review & editing. **Heon-Ho Jeong:** Funding acquisition, Supervision, Project administration, Conceptualization, Writing – original draft, Writing – review & editing.

Declaration of competing interest

The authors declare that they have no known competing financial interests or personal relationships that could have appeared to influence the work reported in this paper.

Data availability

No data was used for the research described in the article.

Acknowledgements

This research was supported by the Basic Science Research Program through the National Research Foundation of Korea (NRF-2020R1C1C1C1005505) funded by the Ministry of Science, ICT and Future Planning (MSIP), Republic of Korea.

Appendix A. Supplementary data

Supplementary data to this article can be found online at https://doi.org/10.1016/j.cej.2024.149377.

References

[1] M.J. Mitchell, M.M. Billingsley, R.M. Haley, M.E. Wechsler, N.A. Peppas, R. Langer, Engineering precision nanoparticles for drug delivery, Nat. Rev. Drug Discov. 20 (2021) 101–124, https://doi.org/10.1038/s41573-020-0090-8.
[2] S. Waheed, Z. Li, F. Zhang, A. Chiarini, U. Armato, J. Wu, Engineering nano-drug biointerface to overcome biological barriers toward precision drug delivery, J. Nanobiotechnol. 20 (2022) 395, https://doi.org/10.1186/s12951-022-01605-4.
[3] Z. Chen, Q. Hu, Z. Gu, Leveraging engineering of cells for drug delivery, Acc. Chem. Res. 51 (2018) 668–677, https://doi.org/10.1021/acs.accounts.7b00526.
[4] J.K. Patra, G. Das, L.F. Fraceto, E.V.R. Campos, M.d.P. Rodriguez-Torres, L. S. Acosta-Torres, L.A. Diaz-Torres, R. Grillo, M.K. Swamy, S. Sharma, Nano based drug delivery systems: recent developments and future prospects, J. Nanobiotechnol. 16 (2018) 1–33, https://doi.org/10.1186/s12951-018-0392-8.
[5] A. Sánchez, S.P. Mejía, J. Orozco, Recent advances in polymeric nanoparticle-encapsulated drugs against intracellular infections, Molecules 25 (2020) 3760, https://doi.org/10.3390/molecules25163760.
[6] A. Zielińska, F. Carreiró, A.M. Oliveira, A. Neves, B. Pires, D.N. Venkatesh, A. Durazzo, M. Lucarini, P. Eder, A.M. Silva, Polymeric nanoparticles: production, characterization, toxicology and ecotoxicology, Molecules 25 (2020) 3731, https://doi.org/10.3390/molecules25163731.
[7] A. Gagliardi, E. Giuliano, E. Venkateswararao, M. Fresta, S. Bulotta, V. Awasthi, D. Cosco, Biodegradable polymeric nanoparticles for drug delivery to solid tumors,

Front. Pharmacol. 12 (2021) 601626, https://doi.org/10.3389/fphar.2021.601626.
[8] H. Wang, R. Li, Y. Rao, S. Liu, C. Hu, Y. Zhang, L. Meng, Q. Wu, Q. Ouyang, H. Liang, Enhancement of the Bioavailability and Anti-Inflammatory Activity of Glycyrrhetinic Acid via Novel Soluplus®—A Glycyrrhetinic Acid Solid Dispersion, Pharmaceutics. 14 (2022) 1797, https://doi.org/10.3390/pharmaceutics14091797.
[9] N. Pathomthongtaweechai, C. Muanprasat, Potential applications of chitosan-based nanomaterials to surpass the gastrointestinal physiological obstacles and enhance the intestinal drug absorption, Pharmaceutics 13 (2021) 887, https://doi.org/10.3390/pharmaceutics13060887.
[10] A. Wicki, D. Witzigmann, V. Balasubramanian, J. Huwyler, Nanomedicine in cancer therapy: challenges, opportunities, and clinical applications, J. Control. Release 200 (2015) 138–157, https://doi.org/10.1016/j.jconrel.2014.12.030.
[11] F.E. Elbassiouni, W.M. El-Kholy, E.-S.-M. Elhabibi, S. Albogami, E. Fayad, Comparative study between curcumin and nanocurcumin loaded PLGA on colon carcinogenesis induced mice, Nanomaterials 12 (2022) 324, https://doi.org/10.3390/nano12030324.
[12] F. da Silva Feltrin, T. Agner, C. Sayer, L.M.F. Lona, Curcumin encapsulation in functional PLGA nanoparticles: A promising strategy for cancer therapies, Adv. Colloid Interface Sci. 300 (2022) 102582. https://doi.org/10.1016/j.cis.2021.102582.
[13] H. Yavarpour-Bali, M. Ghasemi-Kasman, M. Pirzadeh, Curcumin-loaded nanoparticles: A novel therapeutic strategy in treatment of central nervous system disorders, International journal of nanomedicine. (2019) 4449-4460, https://doi.org/10.2147/IJN.S208332.
[14] M. Rai, A.P. Ingle, R. Pandit, P. Paralikar, N. Anasane, C.A.D. Santos, Curcumin and curcumin-loaded nanoparticles: antipathogenic and antiparasitic activities, Expert Rev. Anti Infect. Ther. 18 (2020) 367–379, https://doi.org/10.1080/14787210.2020.1730815.
[15] S. Acharya, S.K. Sahoo, PLGA nanoparticles containing various anticancer agents and tumour delivery by EPR effect, Adv. Drug Deliv. Rev. 63 (2011) 170–183, https://doi.org/10.1016/j.addr.2010.10.008.
[16] M. Szymusiak, X. Hu, P.A.L. Plata, P. Ciupinski, Z.J. Wang, Y. Liu, Bioavailability of curcumin and curcumin glucuronide in the central nervous system of mice after oral delivery of nano-curcumin, Int. J. Pharm. 511 (2016) 415–423, https://doi.org/10.1016/j.ijpharm.2016.07.027.
[17] D.J. Hines, D.L. Kaplan, Poly (lactic-co-glycolic) acid− controlled-release systems: experimental and modeling insights, Critical Reviews™ in Therapeutic Drug Carrier Systems 30 (2013), https://doi.org/10.1615/CritRevTherDrugCarrierSyst.2013006475.
[18] M.H. Leung, A.Q. Shen, Microfluidic assisted nanoprecipitation of PLGA nanoparticles for curcumin delivery to leukemia jurkat cells, Langmuir 34 (2018) 3961–3970, https://doi.org/10.1021/acs.langmuir.7b04335.
[19] S. De, D.H. Robinson, Particle size and temperature effect on the physical stability of PLGA nanospheres and microspheres containing Bodipy, AAPS PharmSciTech 5 (2004) 18–24, https://doi.org/10.1208/pt050453.
[20] O. Escalona-Rayo, P. Fuentes-Vázquez, S. Jardon-Xicotencatl, C.G. García-Tovar, S. Mendoza-Elvira, D. Quintanar-Guerrero, Rapamycin-loaded polysorbate 80-coated PLGA nanoparticles: optimization of formulation variables and in vitro anti-glioma assessment, J. Drug Delivery Sci. Technol. 52 (2019) 488–499, https://doi.org/10.1016/j.jddst.2019.05.026.
[21] B. Shkodra-Pula, C. Grune, A. Traeger, A. Vollrath, S. Schubert, D. Fischer, U. Schubert, Effect of surfactant on the size and stability of PLGA nanoparticles encapsulating a protein kinase C inhibitor, Int. J. Pharm. 566 (2019) 756–764, https://doi.org/10.1016/j.ijpharm.2019.05.072.
[22] I. Seko, H. Tonbul, E. Tavukçuoğlu, A. Şahin, S. Akbas, H. Yanık, S.C. Öztürk, G. Esendagli, M. Khan, Y. Capan, Development of curcumin and docetaxel co-loaded actively targeted PLGA nanoparticles to overcome blood brain barrier, J. Drug Delivery Sci. Technol. 66 (2021) 102867, https://doi.org/10.1016/j.jddst.2021.102867.
[23] A. Gdowski, K. Johnson, S. Shah, I. Gryczynski, J. Vishwanatha, A. Ranjan, Optimization and scale up of microfluidic nanolipomer production method for preclinical and potential clinical trials, J. Nanobiotechnol. 16 (2018) 1–10, https://doi.org/10.1186/s12951-018-0339-0.
[24] J. Ahn, J. Ko, S. Lee, J. Yu, Y. Kim, N.L. Jeon, Microfluidics in nanoparticle drug delivery; From Synthesis to Pre-Clinical Screening, Adv. Drug Deliv. Rev. 128 (2018) 29–53, https://doi.org/10.1016/j.addr.2018.04.001.
[25] A. Aryasomayajula, P. Bayat, P. Rezai, P.R. Selvaganapathy, Microfluidic devices and their applications, Springer handbook of nanotechnology. (2017) 487-536, https://doi.org/10.1007/978-3-662-54357-3_16.
[26] S.S. Murshed, Advances in Microfluidics and Nanofluids, BoD–Books on Demand2021. https://doi.org/10.5772/intechopen.91560.
[27] S.O. Hong, K.-S. Park, D.-Y. Kim, S.S. Lee, C.-S. Lee, J.M. Kim, Gear-shaped micromixer for synthesis of silica particles utilizing inertio-elastic flow instability, Lab Chip 21 (2021) 513–520, https://doi.org/10.1039/D0LC00834F.
[28] J.Y. Han, J.N. La Fiandra, D.L. DeVoe, Microfluidic vortex focusing for high throughput synthesis of size-tunable liposomes, Nat. Commun. 13 (2022) 6997, https://doi.org/10.1038/s41467-022-34750-3.
[29] G. Cai, L. Xue, H. Zhang, J. Lin, A review on micromixers, Micromachines 8 (2017) 274, https://doi.org/10.3390/mi8090274.
[30] K. Ward, Z.H. Fan, Mixing in microfluidic devices and enhancement methods, J. Micromech. Microeng. 25 (2015) 094001, https://doi.org/10.1088/0960-1317/25/9/094001.
[31] T. Zhou, H. Wang, L. Shi, Z. Liu, S.W. Joo, An enhanced electroosmotic micromixer with an efficient asymmetric lateral structure, Micromachines 7 (2016) 218, https://doi.org/10.3390/mi7120218.
[32] Q. Cao, X. Han, L. Li, An active microfluidic mixer utilizing a hybrid gradient magnetic field, Int. J. Appl. Electromagn. Mech. 47 (2015) 583–592, https://doi.org/10.3233/JAE-140057.
[33] H. Van Phan, M.B. Coşkun, M. Şeşen, G. Pandraud, A. Neild, T. Alan, Vibrating membrane with discontinuities for rapid and efficient microfluidic mixing, Lab Chip 15 (2015) 4206–4216, https://doi.org/10.1039/C5LC00836K.
[34] H. Ding, X. Zhong, B. Liu, L. Shi, T. Zhou, Y. Zhu, Mixing mechanism of a straight channel micromixer based on light-actuated oscillating electroosmosis in low-frequency sinusoidal AC electric field, Microfluid. Nanofluid. 25 (2021) 1–15, https://doi.org/10.1007/s10404-021-02430-1.
[35] C. Huang, C. Tsou, The implementation of a thermal bubble actuated microfluidic chip with microvalve, micropump and micromixer, Sens. Actuators, A 210 (2014) 147–156, https://doi.org/10.1016/j.sna.2014.02.015.
[36] S.J. Shepherd, C.C. Warzecha, S. Yadavali, R. El-Mayta, M.-G. Alameh, L. Wang, D. Weissman, J.M. Wilson, D. Issadore, M.J. Mitchell, Scalable mRNA and siRNA lipid nanoparticle production using a parallelized microfluidic device, Nano Lett. 21 (2021) 5671–5680, https://doi.org/10.1021/acs.nanolett.1c01353.
[37] S.J. Shepherd, X. Han, A.J. Mukalel, R. El-Mayta, A.S. Thatte, J. Wu, M.S. Padilla, M.-G. Alameh, N. Srikumar, D. Lee, Throughput-scalable manufacturing of SARS-CoV-2 mRNA lipid nanoparticle vaccines, Proc. Natl. Acad. Sci. 120 (2023), https://doi.org/10.1073/pnas.2303567120 e2303567120.
[38] M.A. Ansari, K.-Y. Kim, K. Anwar, S.M. Kim, A novel passive micromixer based on unbalanced splits and collisions of fluid streams, J. Micromech. Microeng. 20 (2010) 055007, https://doi.org/10.1088/0960-1317/20/5/055007.
[39] D.J. Kang, Effects of channel wall twisting on the mixing in a T-shaped micro-channel, Micromachines 11 (2019) 26, https://doi.org/10.3390/mi11010026.
[40] M. Juraeva, D.-J. Kang, Optimal combination of mixing units using the design of experiments method, Micromachines 12 (2021) 985, https://doi.org/10.3390/mi12080985.
[41] E. Chiesa, M. Bellotti, A. Caimi, B. Conti, R. Dorati, M. Conti, I. Genta, F. Auricchio, Development and optimization of microfluidic assisted manufacturing process to produce PLGA nanoparticles, Int. J. Pharm. 629 (2022) 122368, https://doi.org/10.1016/j.ijpharm.2022.122368.
[42] A. Enders, I.G. Siller, K. Urmann, M.R. Hoffmann, J. Bahnemann, 3D printed microfluidic mixers—a comparative study on mixing unit performances, Small 15 (2019) 1804326, https://doi.org/10.1002/smll.201804326.
[43] S. Movahedirad, Fluid micro-mixing in a passive microchannel: comparison of 2D and 3D numerical simulations, Int. J. Heat Mass Transf. 139 (2019) 907–916.
[44] D. Liu, S. Cito, Y. Zhang, C.F. Wang, T.M. Sikanen, H.A. Santos, A versatile and robust microfluidic platform toward high throughput synthesis of homogeneous nanoparticles with tunable properties, Adv. Mater. 27 (2015) 2298–2304, https://doi.org/10.1002/adma.201405408.
[45] D. Liu, H. Zhang, S. Cito, J. Fan, E. Mäkilä, J. Salonen, J. Hirvonen, T.M. Sikanen, D.A. Weitz, H.l.A. Santos, Core/shell nanocomposites produced by superfast sequential microfluidic nanoprecipitation, Nano Lett. 17 (2017) 606–614, https://doi.org/10.1021/acs.nanolett.6b03251.
[46] T. Baby, Y. Liu, G. Yang, D. Chen, C.-X. Zhao, Microfluidic synthesis of curcumin loaded polymer nanoparticles with tunable drug loading and pH-triggered release, J. Colloid Interface Sci. 594 (2021) 474–484, https://doi.org/10.1016/j.jcis.2021.03.035.
[47] A.D. Aladese, H.-H. Jeong, Recent developments in 3D printing of droplet-based microfluidics, BioChip J. 15 (2021) 313–333, https://doi.org/10.1007/s13206-021-00032-1.
[48] J.L. Sanchez Noriega, N.A. Chartrand, J.C. Valdoz, C.G. Cribbs, D.A. Jacobs, D. Poulson, M.S. Viglione, A.T. Woolley, P.M. Van Ry, K.A. Christensen, Spatially and optically tailored 3D printing for highly miniaturized and integrated microfluidics, Nat. Commun. 12 (2021) 5509, https://doi.org/10.1038/s41467-021-25788-w.
[49] A. Bohr, J. Boetker, Y. Wang, H. Jensen, J. Rantanen, M. Beck-Broichsitter, High-throughput fabrication of nanocomplexes using 3D-printed micromixers, J. Pharm. Sci. 106 (2017) 835–842, https://doi.org/10.1016/j.xphs.2016.10.027.
[50] A. Lavrentieva, T. Fleischhammer, A. Enders, H. Pirmahboub, J. Bahnemann, I. Pepelanova, Fabrication of stiffness gradients of GelMA hydrogels using a 3D printed micromixer, Macromol. Biosci. 20 (2020) 2000107, https://doi.org/10.1002/mabi.202000107.
[51] M. Juraeva, D.-J. Kang, Mixing performance of the modified tesla micromixer with tip clearance, Micromachines 13 (2022) 1375, https://doi.org/10.3390/mi13091375.
[52] C.-C. Hong, J.-W. Choi, C.H. Ahn, A novel in-plane passive microfluidic mixer with modified Tesla structures, Lab Chip 4 (2004) 109–113, https://doi.org/10.1039/B305892A.
[53] S. Hossain, A. Fuwad, K.-Y. Kim, T.-J. Jeon, S.M. Kim, Investigation of mixing performance of two-dimensional micromixer using Tesla structures with different shapes of obstacles, Ind. Eng. Chem. Res. 59 (2020) 3636–3643, https://doi.org/10.1021/acs.iecr.9b06741.
[54] T. Xie, C. Xu, Numerical and experimental investigations of chaotic mixing behavior in an oscillating feedback micromixer, Chem. Eng. Sci. 171 (2017) 303–317, https://doi.org/10.1016/j.ces.2017.05.040.
[55] H.-H. Jeong, B. Lee, S.H. Jin, C.-S. Lee, Hydrodynamic control of droplet breakup, immobilization, and coalescence for a multiplex microfluidic static droplet array, Chem. Eng. J. 360 (2019) 562–568, https://doi.org/10.1016/j.cej.2018.11.182.
[56] C.-T. Wang, Y.-M. Chen, P.-A. Hong, Y.-T. Wang, Tesla valves in micromixers, Int. J. Chem. React. Eng. 12 (2014) 397–403, https://doi.org/10.1515/ijcre-2013-0106.

[57] S. Waheed, J.M. Cabot, N.P. Macdonald, T. Lewis, R.M. Guijt, B. Paull, M. C. Breadmore, 3D printed microfluidic devices: enablers and barriers, Lab Chip 16 (2016) 1993–2013, https://doi.org/10.1039/C6LC00284F.
[58] B. Carnero, C. Bao-Varela, A.I. Gómez-Varela, E. Álvarez, M.T. Flores-Arias, Microfluidic devices manufacturing with a stereolithographic printer for biological applications, Mater. Sci. Eng. C 129 (2021) 112388, https://doi.org/10.1016/j.msec.2021.112388.
[59] F. Subirada, R. Paoli, J. Sierra-Agudelo, A. Lagunas, R. Rodriguez-Trujillo, J. Samitier, Development of a custom-made 3d printing protocol with commercial resins for manufacturing microfluidic devices, Polymers 14 (2022) 2955, https://doi.org/10.3390/polym14142955.
[60] T. Pravinraj, R. Patrikar, Modeling and characterization of surface roughness effect on fluid flow in a polydimethylsiloxane microchannel using a fractal based lattice Boltzmann method, AIP Adv. 8 (2018) 065112, https://doi.org/10.1063/1.5036797.
[61] X. Wang, Z. Liu, Y. Yang, Y. Cai, Q. Song, B. Wang, Effects of sidewall roughness on mixing performance of zigzag microchannels, Chem. Eng. Process.-Process Intensif. 179 (2022) 109057, https://doi.org/10.1016/j.cep.2022.109057.
[62] M. Kim, A. Borhan, Critical conditions for development of a second pair of Dean vortices in curved microfluidic channels, Phys. Rev. E 107 (2023) 055103, https://doi.org/10.1103/PhysRevE.107.055103.
[63] T.S. Sheu, S.J. Chen, J.J. Chen, Mixing of a split and recombine micromixer with tapered curved microchannels, Chem. Eng. Sci. 71 (2012) 321–332, https://doi.org/10.1016/j.ces.2011.12.042.
[64] N. Nivedita, P. Ligrani, I. Papautsky, Dean flow dynamics in low-aspect ratio spiral microchannels, Sci. Rep. 7 (2017) 44072, https://doi.org/10.1038/srep44072.
[65] I. Wong, C.-M. Ho, Surface molecular property modifications for poly (dimethylsiloxane)(PDMS) based microfluidic devices, Microfluid. Nanofluid. 7 (2009) 291–306, https://doi.org/10.1007/s10404-009-0443-4.
[66] D. Wu, Y. Luo, X. Zhou, Z. Dai, B. Lin, Multilayer poly (vinyl alcohol)-adsorbed coating on poly (dimethylsiloxane) microfluidic chips for biopolymer separation, Electrophoresis 26 (2005) 211–218, https://doi.org/10.1002/elps.200406157.
[67] M. Rhee, P.M. Valencia, M.I. Rodriguez, R. Langer, O.C. Farokhzad, R. Karnik, Synthesis of size-tunable polymeric nanoparticles enabled by 3D hydrodynamic flow focusing in single-layer microchannels, Adv. Mater. 23 (2011) H79–H83, https://doi.org/10.1002/adma.201004333.
[68] M. Dutkiewicz, Classification of organic solvents based on correlation between dielectric β parameter and empirical solvent polarity parameter ENT, J. Chem. Soc. Faraday Trans. 86 (1990) 2237–2241, https://doi.org/10.1039/FT9908602237.
[69] R. Stepanyan, J. Lebouille, J. Slot, R. Tuinier, M.C. Stuart, Controlled nanoparticle formation by diffusion limited coalescence, Phys. Rev. Lett. 109 (2012) 138301, https://doi.org/10.1103/PhysRevLett.109.138301.
[70] P. Legrand, S. Lesieur, A. Bochot, R. Gref, W. Raatjes, G. Barratt, C. Vauthier, Influence of polymer behaviour in organic solution on the production of polylactide nanoparticles by nanoprecipitation, Int. J. Pharm. 344 (2007) 33–43, https://doi.org/10.1016/j.ijpharm.2007.05.054.
[71] E. Chiesa, R. Dorati, T. Modena, B. Conti, I. Genta, Multivariate analysis for the optimization of microfluidics-assisted nanoprecipitation method intended for the loading of small hydrophilic drugs into PLGA nanoparticles, Int. J. Pharm. 536 (2018) 165–177, https://doi.org/10.1016/j.ijpharm.2017.11.044.
[72] R. Dinarvand, N. Sepehri, S. Manoochehri, H. Rouhani, F. Atyabi, Polylactide-co-glycolide nanoparticles for controlled delivery of anticancer agents, Int. J. Nanomed. (2011) 877–895, https://doi.org/10.2147/IJN.S18905.
[73] M. Yang, L. Yang, J. Zheng, N. Hondow, R.A. Bourne, T. Bailey, G. Irons, E. Sutherland, D. Lavric, K.-J. Wu, Mixing performance and continuous production of nanomaterials in an advanced-flow reactor, Chem. Eng. J. 412 (2021) 128565, https://doi.org/10.1016/j.cej.2021.128565.
[74] P. Erfle, J. Riewe, H. Bunjes, A. Dietzel, Goodbye fouling: A unique coaxial lamination mixer (CLM) enabled by two-photon polymerization for the stable production of monodisperse drug carrier nanoparticles, Lab Chip 21 (2021) 2178–2193, https://doi.org/10.1039/D1LC00047K.
[75] H. Xia, Y. Seah, Y. Liu, W. Wang, A.G. Toh, Z. Wang, Anti-solvent precipitation of solid lipid nanoparticles using a microfluidic oscillator mixer, Microfluid. Nanofluid. 19 (2015) 283–290, https://doi.org/10.1007/s10404-014-1517-5.
[76] K. Abstiens, A.M. Goepferich, Microfluidic manufacturing improves polydispersity of multicomponent polymeric nanoparticles, J. Drug Delivery Sci. Technol. 49 (2019) 433–439, https://doi.org/10.1016/j.jddst.2018.12.009.
[77] P.M. Valencia, E.M. Pridgen, M. Rhee, R. Langer, O.C. Farokhzad, R. Karnik, Microfluidic platform for combinatorial synthesis and optimization of targeted nanoparticles for cancer therapy, ACS Nano 7 (2013) 10671–10680, https://doi.org/10.1021/nn403370e.
[78] L. Capretto, D. Carugo, S. Mazzitelli, C. Nastruzzi, X. Zhang, Microfluidic and lab-on-a-chip preparation routes for organic nanoparticles and vesicular systems for nanomedicine applications, Adv. Drug Deliv. Rev. 65 (2013) 1496–1532, https://doi.org/10.1016/j.addr.2013.08.002.
[79] M.M. Yallapu, B.K. Gupta, M. Jaggi, S.C. Chauhan, Fabrication of curcumin encapsulated PLGA nanoparticles for improved therapeutic effects in metastatic cancer cells, J. Colloid Interface Sci. 351 (2010) 19–29, https://doi.org/10.1016/j.jcis.2010.05.022.
[80] C.J.M. Rivas, M. Tarhini, W. Badri, K. Miladi, H. Greige-Gerges, Q.A. Nazari, S.A. G. Rodríguez, R.Á. Román, H. Fessi, A. Elaissari, Nanoprecipitation process: From encapsulation to drug delivery, Int. J. Pharm. 532 (2017) 66–81, https://doi.org/10.1016/j.ijpharm.2017.08.064.
[81] E.Y. Makhani, A. Zhang, J.B. Haun, Quantifying and controlling bond multivalency for advanced nanoparticle targeting to cells, Nano Convergence 8 (2021) 1–23, https://doi.org/10.1186/s40580-021-00288-1.
[82] D.R. Elias, A. Poloukhtine, V. Popik, A. Tsourkas, Effect of ligand density, receptor density, and nanoparticle size on cell targeting, Nanomed. Nanotechnol. Biol. Med. 9 (2013) 194–201, https://doi.org/10.1016/j.nano.2012.05.015.
[83] K. Kita, C. Dittrich, Drug delivery vehicles with improved encapsulation efficiency: taking advantage of specific drug–carrier interactions, Expert Opin. Drug Deliv. 8 (2011) 329–342, https://doi.org/10.1517/17425247.2011.553216.
[84] Y. Liu, G. Yang, S. Jin, L. Xu, C.X. Zhao, Development of high-drug-loading nanoparticles, ChemPlusChem 85 (2020) 2143–2157, https://doi.org/10.1002/cplu.202000496.
[85] G.H. Diering, M. Numata, Endosomal pH in neuronal signaling and synaptic transmission: role of Na+/H+ exchanger NHE5, Front. Physiol. 4 (2014) 412, https://doi.org/10.3389/fphys.2013.00412.
[86] B.S. Zolnik, D.J. Burgess, Effect of acidic pH on PLGA microsphere degradation and release, J. Control. Release 122 (2007) 338–344, https://doi.org/10.1016/j.jconrel.2007.05.034.
[87] J. Kaur, R.R. Singh, E. Khan, A. Kumar, A. Joshi, Piperine-loaded PLGA nanoparticles as cancer drug carriers, ACS Appl. Nano Mater. 4 (2021) 14197–14207, https://doi.org/10.1021/acsanm.1c03664.
[88] J. Zhao, H. Yang, J. Li, Y. Wang, X. Wang, Fabrication of pH-responsive PLGA (UCNPs/DOX) nanocapsules with upconversion luminescence for drug delivery, Sci. Rep. 7 (2017) 18014, https://doi.org/10.1038/s41598-017-16948-4.
[89] A.D. Aladese, H.-H. Jeong, Numerical and experimental investigations of uniform fluid distribution for droplet formation in parallelized microfluidics, Front. Sens. 3 (2022) 1014864, https://doi.org/10.3389/fsens.2022.1014864.